

Multijunction Concentrator Solar Cells: Analysis and Fundamentals

Eduardo F. Fernández, Antonio J. García-Loureiro
and Greg P. Smestad

Abstract Multijunction (MJ) concentrator solar cells are primarily constructed of III-V semiconductor materials. The high solar-conversion efficiencies of these devices are dependent on precise control of growth conditions using one of several techniques such as molecular beam epitaxy, metal organic chemical vapour, or metal organic vapour-phase epitaxy deposition. The use of several junctions in an MJ tandem stack allows these devices to achieve efficiencies that are not possible for single-junction devices. Their behaviour is consequently complex, but it can be understood through an examination of the external quantum efficiency and the temperature dependence of each cell in the stack. This chapter lays out a systematic approach for understanding the spectral and temperature dependence of the overall MJ device by way of consideration of its component subcells. The efficiency of the cell as a function of temperature and concentration is described for both lattice-matched and metamorphic triple-junction (TJ) solar cells. The electrical characteristics and current–voltage curves are described from these considerations, and the performance of MJ solar cells under real operating conditions are then presented by considering a term describing the overall thermal factor and another term for the spectral factor. These terms can be understood from the background presented in the previous sections. Finally, the power output for the complete cell incorporated into a Fresnel lens based high-concentration photovoltaic system is presented for a particular geographic location using meteorological data.

1 Introduction

Multijunction (MJ) solar cells comprised of III-V materials are routinely used in space applications, for example, on satellites, unmanned space probes, planetary landers, and the International Space Station (ISS) [1, 2]. In contrast, when these

E.F. Fernández (✉) · A.J. García-Loureiro
University of Santiago de Compostela, Santiago de Compostela, Spain
e-mail: eduarferfer@gmail.com

G.P. Smestad
Sol Ideas Technology Development, San José, California, USA

© Springer International Publishing Switzerland 2015
P. Pérez-Higueras and E.F. Fernández (eds.), *High Concentrator Photovoltaics*,
Green Energy and Technology, DOI 10.1007/978-3-319-15039-0_2

solar cells are used for terrestrial applications, they are used together with concentrator optics so that the cell cost becomes a small fraction of the overall system cost. This creates several challenges to overcome that stem from the increase in the irradiance on, and temperature of, the cell [3–5]. The MJ solar cell approach offers significant advantages and disadvantages that can only be understood by analysing a given design’s composition and performance from a fundamental perspective. This is the goal of this chapter.

An MJ solar cell is a quantum solar converter based on the use of two or more subsolar cells (subcells) comprised of semiconductor materials with different energy gaps (i.e., band-gaps, E_{gap}). It can take the form of a spectral splitting system [1, 4, 5] or stacked tandem junctions. Both approaches can be accomplished by using different stoichiometric semiconductor materials or by varying the composition of semiconductor alloys. An example of a stacked tandem device was first introduced in the late 1970s. It used two subcells each with a p–n junction: The bottom cell was based on gallium arsenide (GaAs) and the top cell (exposed to sunlight) was based on aluminium gallium arsenide. A different approach was later developed by the National Renewable Energy Laboratory based on an indium gallium phosphide (or InGaP alloy) junction on top of a GaAs middle junction grown on a germanium (Ge) substrate. This formed a triple-junction (TJ) tandem cell [1–5]. Further refinements replaced the GaAs with InGaAs alloys. The stacked-subcell approach has resulted in MJ cells of >40 % solar conversion efficiency [6–8]. Further work includes quantum well and quantum dot layers as well as inverted metamorphic (IMM) TJ solar cells [1, 9]. Combinations of GaAs and GaSb have also shown promise [5].

The basic idea in all such MJ cells is to improve the solar conversion efficiency, η , of the whole solar cell by optimizing the light absorption and photocurrent generation of each subcell for a narrow wavelength range. As shown in Table 1, a single-junction (SJ) solar cell, built with only one light-absorber material, has a maximum theoretical (thermodynamic) efficiency at a one-sun concentration of 30–34 % in sunlight. To improve on this efficiency, it is necessary to concentrate the sunlight on the cell and/or to interconnect several subcells. The efficiency limit increases to approximately 86.8 % for an infinite number of subcells at the maximum concentration ratio that can be achieved on Earth [10, 11].

Table 1 is for a cell temperature of 298 K. If the cell temperature increases beyond this, thermodynamics requires that the cell voltage decreases [12, 13]. An approximate relationship holds for the open circuit voltage, V_{oc} , at a given temperature, T , as follows:

$$\frac{d(qV_{\text{oc}})}{dT} = - \frac{E_{\text{gap}} - qV_{\text{oc}}}{T} \quad (1)$$

Here, q is the charge on an electron. In actual solar cells, this temperature dependence often leads to solar conversion efficiencies that are lower at greater cell temperatures. The temperature dependence of several key cell parameters will be the topic of subsequent chapters.

Table 1 The maximum solar conversion efficiency for tandem cells as a function of the number of subcells in the stack, n , for different concentration ratios, X [10, 11]

Concentration ratio (X)	No. of cells in the stack (n)	Maximum efficiency (η)
1	1	31.0
	2	42.9
	3	49.3
	...	—
	∞	68.2
100	1	35.2
	2	48.4
	3	55.6
	...	—
	∞	76.2
46,300	1	40.8
	2	55.7
	3	63.9
	...	—
	∞	86.8

The theoretical analysis assumes blackbody radiation for the sun, rather than the AM1.5 standard solar spectrum, but the general results (and the efficiency values) are quite similar if the actual solar spectrum is considered

Although the efficiencies obtained in actual cells are noteworthy and have improved over time, there exists a considerable gap between theoretical and experimental values. This is due to one or more loss mechanisms operating in solar cells. For example, not every photon that a subcell absorbs gives rise to an electron-hole pair that is collected at the electrical contacts. This is reflected by an external quantum efficiency (EQE) that is less than unity [1, 4, 6]. In addition, there are both optical losses, such as those from parasitic absorption by interconnection layers, and electrical losses, such as those caused by internal series and shunt resistance. In the section that follows, an overview of MJ concentrator solar cells is presented, and the precise growth conditions necessary to create MJ devices are outlined. Then an analysis of the whole MJ cell will be presented that allows one to characterize and understand the losses of a particular design. This leads to the ability to predict the performance of MJ cells under the actual conditions found under deployment in a high-concentrator photovoltaics (HCPV) system.

2 Overview of MJ Concentrator Solar Cells

The key to the success of modern III-V solar cells is based on the development of advanced growth technologies, mainly molecular beam epitaxy, metal organic chemical vapour deposition, metal organic vapour phase epitaxy and other similar techniques [14–17]. It is necessary to have high-accuracy epitaxial growth to obtain

a highly efficient MJ solar cell. This means that there is little difference between the lattice constants of adjacent layers. The growth techniques allow for unprecedented control on the atomic level of the semiconductor devices. This makes it possible to grow new materials, including pseudomorphic and alloy multiple compositions, for example, $\text{Si}_x\text{Ge}_{1-x}$, $\text{Al}_x\text{Ga}_{1-x}\text{As}$, or $\text{In}_x\text{Ga}_{1-x}\text{As}$, where x is the mole fraction that specifies the composition of the alloy [18]. It is necessary to consider that the alloy components are distributed uniformly over the whole layer without any type of clustering. This is reasonable in the case of solar cells due to the dimension of the active region of these devices compared with the lattice constant.

A semiconductor material has many types of properties [19–22], but the most relevant considerations in the design of an efficient MJ solar cell are the energy gap and the lattice constant. The energy gap is equivalent to the energy that is necessary to free a bond electron in the crystal, thereby creating a hole in the valance band and an electron in the conduction band. In this case, it corresponds to the minimum energy of the photon to be absorbed for the semiconductor material. The lattice constant is the physical dimension of the unit cell in the crystal lattice of the semiconductor. The ideal situation should be that the different materials of multi-layer semiconductor devices have the same lattice constant, or at least as close as possible, to decrease the number of defects and thermal, mechanical, and electrical stresses. The results of such stresses are recombination centers within the band-gap that lead to efficiency losses. In most cases, it is not a trivial matter to grow a mechanically and electrically stable solar cell, and thus it is necessary to consider a critical thickness of the semiconductor layer that corresponds to the maximum thickness of the material necessary to avoid dislocations and similar defects that can act as recombination centres [23]. Figure 1 shows the energy gap versus lattice constant for several elements and alloy materials [24]. In the case of an alloy composition of three or more materials—as in $\text{Al}_x\text{Ga}_{1-x}\text{As}$, $\text{In}_x\text{Ga}_{1-x}\text{P}$, or $\text{Ga}_x\text{In}_{1-x}\text{As}_y\text{P}_{1-y}$ with two molar fractions, x and y —the lattice constant and the energy band-gap of the resulting material is a complex function of the mole fraction.

An MJ solar cell with two, three, or more junctions is a set of the same number of p–n junctions made from different materials, stacked on the top of each other, including metallic contacts on the top and bottom of the solar cell [25–27]. The idea

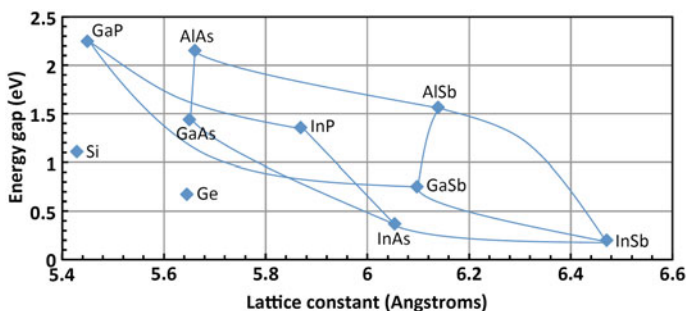


Fig. 1 Energy band-gap versus lattice constant for several semiconductors used in MJ HCPV cells

is to subdivide the incident solar spectrum into several parts to be absorbed for the different subsolar cells; each one has an optimized efficiency for a certain range of wavelengths in the spectrum of the incident sunlight. The goal is to find the best and most advantageous band-gap combination for each subsolar cell to convert the total incident solar light with the maximum possible efficiency. It is also necessary to take into account low-resistance metal contacts for obtaining a high-efficiency solar cell. There are several possibilities to connect the different p–n junctions, but one of the most efficient methods is to use a tunnel junction with very low resistance and very thin layers to decrease, as much as possible, the absorbed light in these layers [28]. In addition to all of the previously mentioned factors, one should not overlook the importance of the semiconductor materials and the thickness of the various subcells as part of the design. This is necessary to obtain the best current balance among all of the subcells. The ideal situation is when all of the subcells generate the same light-generated current under the relevant spectral conditions outdoors. However, there is inevitably a subcell of the MJ with the lowest current, which limits the total current of the MJ because the p–n junctions are connected in series [29]. The total device voltage is the sum of the voltage of each subcell minus the voltage of the tunnel junctions because they are in reverse bias. A typical structure of a TJ solar cell is depicted in Fig. 2. In this case, each subcell is based on several materials with different band-gaps. The p–n solar cell with the highest band-gap is located on the top of the MJ solar cell stack to absorb the highest-energy photons, and the other subcells are placed in decreasing order of the band-gap with the aim to capture photons with less energy (longer wavelengths). The plot shows the air mass (AM) 1.5 direct (AM1.5D, ASTM G-173-03) reference spectrum [30] with the dashed vertical lines indicating the band-gaps for the top [gallium indium

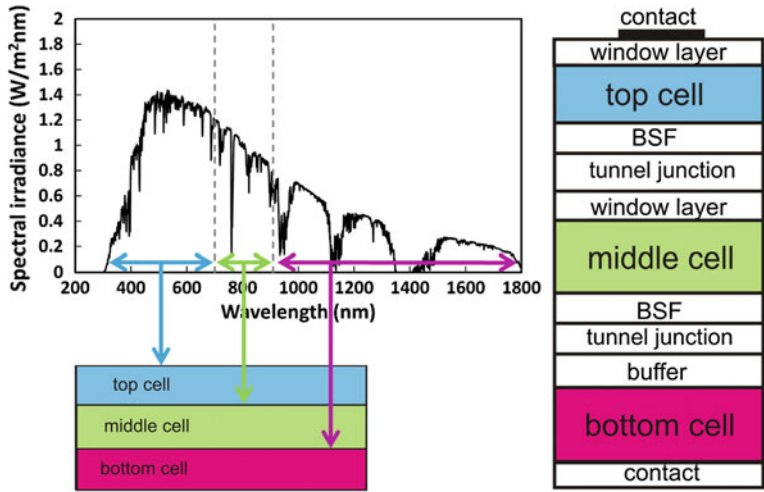


Fig. 2 Portions of the solar spectrum absorbed in a TJ solar cell (*left*) and a schematic of a typical monolithic TJ HCPV solar cell (*right*)

phosphide (GaInP; 1.88 eV)] and middle [gallium indium arsenide (GaInAs) (1.41 eV)] subcells. The bottom subcell in this example is Ge (0.67 eV). Absorption of the photons is determined by the energy gap of the semiconductor material alloy and its absorption coefficient [19]. The latter parameter indicates how far into material photons of a specific energy can penetrate before they are absorbed by the material. To improve the efficiency of the MJ solar cell, each one is designed to absorb only one part of the spectrum of sunlight (e.g., AM1.5D). Window layers should be included on the top subcells to decrease the surface recombination velocity, and a back surface field (BSF) layer should also be used to minimize scattering and loss of charge carriers at the tunnel junction [31]. It is necessary that both layers should be as transparent as possible so the photons can be absorbed in the active regions of the device. This is shown in Fig. 2 (right side).

One of the main problems of the MJ solar cell is related to the various lattice constants of the semiconductor alloy material of each layer and the need to grow an MJ solar cell when several materials with different lattice constants are necessary to obtain the highest overall device efficiency. If the materials of the separate p–n junctions have the same lattice constant, then it is easier to grow the MJ solar cell. In this approach, the cells are called lattice-matched (LM) cells. [32]. The main disadvantage of this strategy is that the materials with different band-gaps selected for the subcells should have the same, or a very close, lattice constant. This constraint decreases maximum efficiency because it is not possible to select the best materials for each subcell in terms of band-gap. One approach to increase the number of possible semiconductor materials that can be selected is to use materials with different lattice constants but with thin layers to decrease the stress in the structure. These solar cells are called metamorphic-mismatched (MM) cells. This option increases the list of possible materials that can be used, but it still limits the flexibility to select the best materials for the subcells. This problem is critical when four or more different materials with several lattice constants are necessary to create an MJ solar cell [33].

There is another device structure called inverted-metamorphic (IMM) [34–36]. In this case, the MJ solar cell is grown in an inverted order on a suitable substrate starting with the top subcell. Later, the original growth substrate is removed, and the front metallic contact is deposited on the top layer [37]. In addition, more flexible techniques exist that use materials with different lattice constants. For example, it is possible to mechanically stack cells to connect several separate subcells or use fabrication by way of wafer bonding [38–40]. This last method combines semiconductor materials with different lattice constants by forming semiconductor bonds at the common interface layer. Each subcell, or group of subcells, are grown on different substrates and then joined together. Afterward, the substrate of the top cell is removed. For this process to succeed, it is necessary to have high-quality, low-roughness surfaces. A good example of this technique is a four-junction device comprised of GaInP/GaAs/gallium indium arsenide phosphide (GaInAsP)/GaInAs, which has an efficiency of approximately 45 % [41].

In the case of the application of the device in an HCPV system, optimization of the front metal grid pattern is essential for a specific irradiance level and solar concentration (i.e., $500\times$ to $1000\times$). The main objective is to maximize light absorption and decrease, as much as possible, the ohmic and shadow losses generated for the metal grid [31]. The design and analysis of MJ solar cells begins with this criterion and by considering their behaviour versus the input solar spectrum, temperature, and electrical properties.

3 Analysis of the Behaviour of MJ Solar Cells

The behaviour of MJ solar cells is inherently different than that of conventional SJ solar cells. The internal series connection of several junctions with different band-gaps makes these devices more sensitive to incident spectral irradiance. In addition, the electrical parameters and temperature dependencies are significantly influenced by the irradiance level. In this section, the basic aspects for understanding the performance of MJ solar cells under different operating regimes are presented.

3.1 EQE

The external quantum efficiency (EQE) offers valuable information for understanding the performance of a solar cell. The EQE, as a function of wavelength, represents the ratio of the number of electrons collected at the external contacts of the cell to the number of incident photons as follows:

$$\text{EQE}(\lambda) = \frac{\text{number of electrons}}{\text{number of photons}(\lambda)} \quad (2)$$

The wavelength interval for measurements of EQE (λ) typically ranges from 1 to 10 nm. EQE can be related to the spectral response (SR). The SR represents the amperes generated per watt of incident light of a given wavelength and can be expressed as follows:

$$\text{SR}(\lambda) = \frac{q\lambda}{hc} \text{EQE}(\lambda) \quad (3)$$

where q is the electric charge, λ is the wavelength, h is Planck's constant, and c is the speed of light. Given this relationship, the short-current density (J_{sc}) of a cell for a particular spectral distribution $E(\lambda)$ can be estimated as follows:

$$J_{sc} = \int SR(\lambda)E(\lambda)d\lambda \quad (4)$$

The J_{sc} is measured at the point at the I-V curve where $V = 0$ and is typically expressed in mA/cm^2 . The standard (or reference) spectral distribution for AM1.5D is shown in Fig. 2. However, as will be described in a subsequent chapter, the actual spectral distribution under the operating conditions found for an MJ cell used in a deployed (real-world) HCPV system is a function of the location of the system as well as the time of year and time of day.

As discussed previously, to improve the conversion efficiency, MJ solar cells are based on several junctions interconnected in series in which each subcell responds to a particular band of the spectrum. Because of this, the short-current density of an MJ solar cell is the subcell with the lowest current. This is usually expressed as follows:

$$J_{sc} = \min \left(\int SR_i(\lambda)E(\lambda)d\lambda \right) \quad (5)$$

where the index i represents the junction, or subcell, considered in the MJ solar cell.

Figure 3 shows the EQE, at 25 and 75 °C, of an LM GaInP/GaInAs/Ge solar cell as an example of the number of photons collected in each spectral band of a typical MJ solar cell. This plot shows the EQE's variation with temperature. As can be seen, the absorption range is mainly determined by the band-gap. Because of this, the key to understanding the variations of EQE with temperature is by considering the change of the band-gap energy (E_{gap}) versus temperature. This variation can be explained with the Varshni relation as shown [42]:

$$E_{gap}(T) = E_{gap}(0) - \frac{\alpha T^2}{T + \beta} \quad (6)$$

where $E_{gap}(0)$ is the band-gap energy at 0 K, and α and β are material constants. The Eq. (6) shows that the energy gap decreases as the temperature increases. Hence, as the device temperature increases, the MJ solar cell is able to absorb photons with lower energy. This explains the shift in EQE for the top, middle and bottom junctions at longer wavelengths as shown in Fig. 3. In addition, a loss in EQE for the middle and bottom junctions at shorter wavelengths is also observed. This can be mainly explained due to the gain in EQE at longer wavelengths by the junction directly above. This effect is also observed to a lesser degree in the EQE of the top junction, probably due to the decrease with temperature of the band-gap energy of the window layer of the MJ solar cell [43, 44].

The effect of temperature on the EQE described previously clearly suggests that the influence of temperature on the electrical parameters of an MJ solar cell is more complex than in an SJ device. The J_{sc} of the current-limiting junction increases with temperature due to the decrease of its energy gap. However, this increase is lessened by the effect of the junction immediately above because the current of this

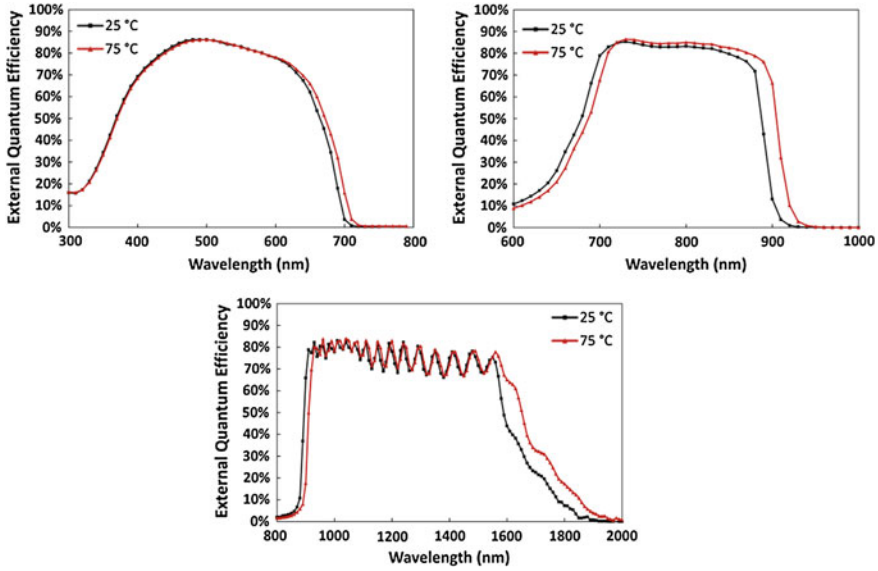


Fig. 3 Experimental EQE of the top junction (*top left*), middle junction (*top right*), and bottom junction (*bottom*) of an LM GaInP/GaInAs/Ge TJ solar cell at 25 and 75 °C [48, 49]. The oscillations in the external quantum efficiency for the Ge subcell are due to optical interference effects from the many thin layers above it [50, 51]

junction is also increased with temperature. Bearing this in mind, the temperature coefficient of an MJ solar cell (dJ_{sc}/dT) can be expressed as follows [45]:

$$\frac{dJ_{sc}}{dT} = \frac{dJ_{sc,i}}{dT} - \frac{dJ_{sc,i-1}}{dT} \quad (7)$$

where $(dJ_{sc,i}/dT)$ and $(dJ_{sc,i-1}/dT)$ are the temperature coefficient of the limiting-junction and the temperature coefficient of the junction above, respectively. This phenomenon implies that (dJ_{sc}/dT) depends on the incident spectrum and that the temperature coefficient of the whole MJ cell could not be always positive. At the same time, the I-V characteristics of an MJ solar cell are strongly affected by the current balance among the junctions. Hence, the influence of temperature on the rest of the electrical parameters is also expected to be affected by the incident spectral distribution and the limiting junction [46, 47].

3.2 Influence of the Input Spectrum

It is well known that MJ solar cells have a larger spectral dependence than SJ solar cells because of the series connection of several subcells with different energy gaps

[52]. This is shown graphically in Fig. 2. Taking this into account, the temperature dependence of the electric parameters of an MJ solar cell are also expected to be influenced by the incident spectrum as was previously commented on. To clarify this issue, Fig. 4 shows the main electrical parameters of an LM GaInP/GaInAs/Ge solar cell under illumination by different spectra at 25 and 75 °C. The spectra are expressed through the spectral matching ratio (SMR) index for the top and middle subcells as shown [53]:

$$SMR(top/middle) = \frac{J_{L,top}}{J_{L,top}^{1.5D}} / \frac{J_{L,middle}}{J_{L,middle}^{1.5D}} \quad (8)$$

where $J_{L,top}$ and $J_{L,middle}$ are the photo current densities of the top and middle junctions, respectively. Figure 4 (top left) shows J_{sc} versus SMR for the two temperatures. A maximum at $SMR = 1$ can be seen. This maximum represents the spectral condition where the top and middle subcells generate the same current (current-matched condition). Around this point, J_{sc} decreases due to the current limitation in one of the subcells. On the left side of the maximum, the current of the middle subcell is increased, whereas the current of the top subcell is decreased. This corresponds to red-rich spectra, and the top subcell is limiting the current ($SMR < 1$). On the right side of the maximum, the current of the top subcell is increased, whereas the current of the middle subcell is decreased. Hence, these

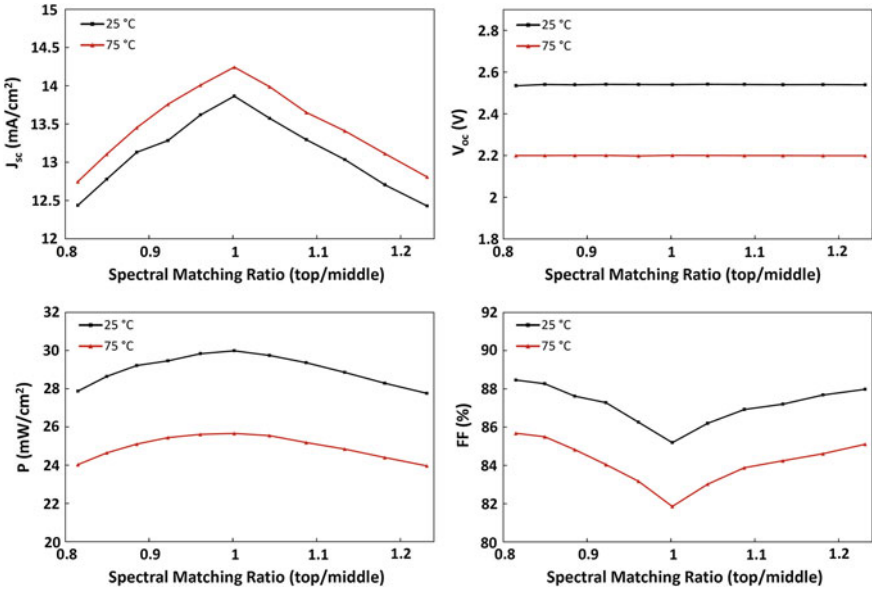


Fig. 4 Experimental short-circuit current density (J_{sc}), open-circuit voltage (V_{oc}), P , and FF versus SMR for the top and middle subcells at 25 and 75 °C of an LM GaInP/GaInAs/Ge solar cell. $SMR = 1$ corresponds to AM1.5D, ASTM G173-03, 1000 W/m² where the three subcells generate the same current as under reference conditions [55, 56]

spectral conditions are more blue-rich, and the middle subcell is limiting the current ($SMR > 1$). Related to temperature, the cell shows an increase in current with temperature more or less independent of the SMR. The open-circuit voltage (V_{oc}) versus SMR for the two temperatures is shown in Fig. 4 (top right). As can be seen, no significant dependence on incident spectrum is found. In addition, the cell shows a decrease in open-circuit voltage with a temperature independent of the SMR. Figure 4 (bottom left) shows the maximum power density (P) versus SMR for the two temperatures. P shows a similar behaviour to J_{sc} under spectral changes. A maximum in P at $SMR = 1$ can be observed. In addition, around the maximum, P decreases due to the current limitation by one of the subcells. Regarding temperature, the cell again shows a decrease in temperature more or less independent of the spectral changes. The fill factor (FF) versus SMR for the two temperatures is given in Fig. 4 (bottom right). In this case, FF shows the opposite behaviour compared with J_{sc} and P under spectral changes but with less variation. There is a minimum at $SMR = 1$, and the FF increases around it. As for the previous parameter, the cell shows a decrease in temperature more or less independent of the spectral changes. The different behaviour of the FF under spectral changes can be explained by analysing the relationship between FF and the rest of the electrical parameters as follows:

$$FF = \frac{P}{J_{sc} V_{oc}} \quad (9)$$

V_{oc} can be considered independent of incident spectrum as a first approximation. At the same time, J_{sc} shows a larger spectral influence than P . Hence, the FF grows when J_{sc} decreases because P decreases to a lesser extent under spectral changes. This behaviour exhibited by the FF under spectral variations can be used as a tool to evaluate the current-matching among the subcells of an MJ solar cell under operating conditions [54].

As presented, the electrical parameters of an MJ solar cell are strongly influenced by the spectral distribution. However, the temperature dependences of MJ solar cell parameters can be considered independent of spectrum with a low margin of error [49, 55, 57].

3.3 Influence of Optical Concentration

MJ solar cells show an important spectral dependence as was previously commented on. In addition to this, the I-V parameters of MJ concentrator solar cells are also affected by the illumination level. Furthermore, the temperature coefficients of the electrical parameters are also affected by the optical concentration under operating conditions [58].

Under uniform irradiance, the short-circuit current can be considered linear with respect to the concentration and is usually expressed as:

$$I_{sc} = X \cdot I_{sc,1 \text{ sun}} \quad (10)$$

where X is the concentration factor or effective concentration, and $I_{sc,1 \text{ sun}}$ is the short-circuit current at one sun (1000 W/m^2). The concentration factor is sometimes called the “concentration ratio” and is given the symbol “ C ” in some texts. Accordingly, the absolute temperature coefficient of I_{sc} can be expressed as a function of concentration as follows:

$$\frac{dI_{sc}}{dT} = X \frac{dI_{sc,1 \text{ sun}}}{dT} \quad (11)$$

The rest of the electrical parameters and temperature coefficients show a more complex relationship versus concentration. To clarify this point, Fig. 5 shows the main electrical parameters of an LM GaInP/GaInAs/Ge solar cell under different concentration levels at 25 and 65 °C.

Figure 5 (top) shows V_{oc} versus concentration for the two temperatures. As can be seen, V_{oc} grows with a logarithmic dependence as the concentration increases. For subcells connected in series, this dependence can be expressed as [57]:

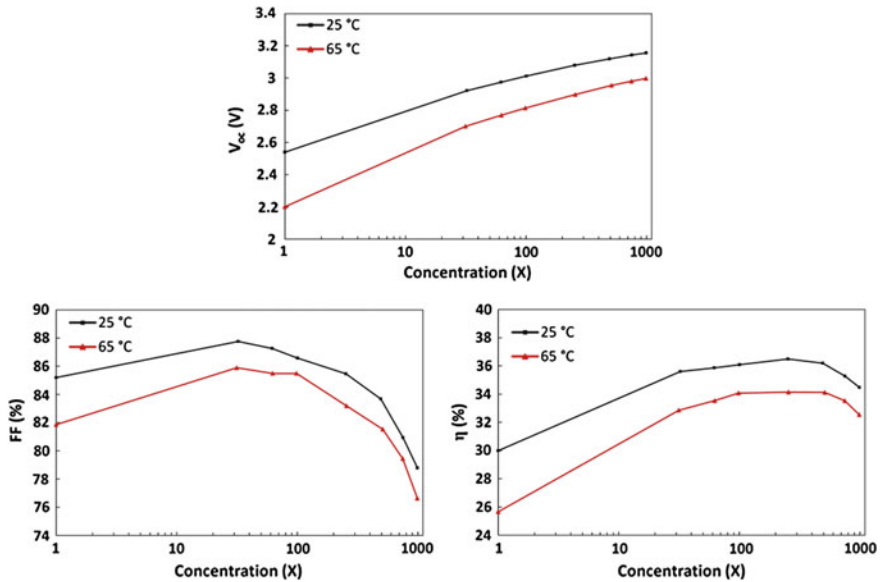


Fig. 5 Experimental open-circuit voltage (V_{oc}), FF, and efficiency (η) versus concentration (X) at 25 and 65 °C of an LM GaInP/GaInAs/Ge solar cell [61, 62]. The front metal grid of the cell is optimized for operating at concentrations between 250 \times and 500 \times

$$V_{oc} = \sum_{i=1}^n V_{oc,i,1 \text{ sun}} + \frac{kT}{q} \sum_{i=1}^n m_i \ln(X) = V_{oc,1 \text{ sun}} + \frac{mkT}{q} \ln(X) \quad (12)$$

where n is the number of subcells in series, $V_{oc,1 \text{ sun}}$ is the open-circuit voltage at one sun, m is the diode ideality factor, k is Boltzmann's constant, and q is the electric charge. As is also shown in Fig. 5 (top), the temperature dependence of V_{oc} decreases with concentration. This can be explained by writing Eq. (11) as follows:

$$\frac{dV_{oc}}{dT} = \frac{dV_{oc,1 \text{ sun}}}{dT} + \frac{mk}{q} \ln(X) \quad (13)$$

The first term on the right, which is the temperature coefficient at one sun, is negative. The second term on the right is positive and increases with concentration such that the temperature coefficient of V_{oc} decreases in absolute value versus concentration. It is important to note that to know V_{oc} and dV_{oc}/dT at a particular concentration ratio from their values at one sun, the value of the ideality factor should be known. Reported ideality factors for TJ solar cells are usually in the range 3–4 for concentration levels from $1\times$ to $1000\times$ [58]. The ideality factor is influenced by the recombination mechanism and the concentration ratio (which determines the injection level) [59]. The dominant recombination mechanism for an MJ solar cell has been shown to be different at low and high irradiance levels. The trend is toward the radiative limit ($m = 1$ for each subcell) as concentration increases [57, 60]. Because of this, it is necessary to perform an analysis of m as a function of concentration [$m = m(X)$] to accurately predict V_{oc} and dV_{oc}/dT . This behaviour can be seen in the change and decrease of the slope of V_{oc} as a function of $\ln(X)$ shown in Fig. 5 (top).

Figure 5 (bottom left) shows the FF versus concentration for the two temperatures. As can be seen, the FF increases with concentration $\leq 30\times$. Above this point, the FF decreases gradually due to series resistance losses. As in the previous case, the temperature dependence of FF decreases with concentration. This can be explained by writing the temperature coefficient of the FF as [45]:

$$\frac{dFF}{dT} = \frac{\ln(V_{oc,1 \text{ sun}} \frac{qT}{mkT} + \ln(X) + 1) \left(\frac{dV_{oc,1 \text{ sun}}}{dT} \frac{q}{mkT} - V_{oc,1 \text{ sun}} \frac{q}{mkT^2} \right)}{(V_{oc,1 \text{ sun}} \frac{q}{mkT} + \ln(X) + 1)^2} \quad (14)$$

This equation expresses the variation of the temperature coefficient for FF with concentration assuming a negligible series resistance. As shown, the numerator is negative and grows in absolute value with concentration. However, the denominator increases to a larger extent with concentration. As a result, dFF/dT decreases in absolute value with concentration, and this explains the behaviour described previously.

Figure 5 (bottom right) shows the efficiency (η) versus concentration for the two temperatures. As can be seen, η increases with concentration until $>250\times$. This

increase is dominated by the logarithmic increase of V_{oc} with the intensity of the light. However, as the concentration increases, this effect is counterbalanced by the decrease of the FF due to series resistance losses. As a result, the efficiency is decreased above a certain concentration level. As in the previous cases, the temperature dependence of η is decreased with concentration. This can be explained by writing the temperature coefficient of η as shown [61]:

$$\frac{1}{\eta} \frac{d\eta}{dT} = \frac{1}{V_{oc}} \frac{dV_{oc}}{dT} + \frac{1}{FF} \frac{dFF}{dT} + \frac{1}{I_{sc}} \frac{dI_{sc}}{dT} \quad (15)$$

The temperature coefficients of V_{oc} and FF decrease with concentration, whereas the temperature coefficient of I_{sc} is kept constant. Furthermore, in Eq. (15), the dominant term is the temperature coefficient of V_{oc} . Hence, the temperature coefficient of η should decrease with concentration and will be mainly given by the temperature coefficient of V_{oc} as follows:

$$\frac{1}{\eta} \frac{d\eta}{dT} \approx \frac{1}{V_{oc}} \frac{dV_{oc}}{dT} \quad (16)$$

It is important to note that this approximation may not be valid at increased concentration levels due to the strong decrease of dV_{oc}/dT as discussed in the literature [45]. However, experimental results show that the temperature coefficient of η can be approximated using Eq. (16) with a low margin of error until concentration levels reach even the extreme values of $10,000\times$ [60].

Table 2 shows an example of the relative temperature coefficients of η and V_{oc} of an LM and MM TJ solar cell at different concentration levels. As was discussed, the temperature coefficients of V_{oc} and η are similar and decrease with concentration for both types of MJ solar cells. In addition, the MM solar cell shows a slightly greater temperature dependence than the LM solar cell.

Table 2 Experimental temperature coefficients of η and V_{oc} of an LM and an MM GaInP/GaInAs/Ge TJ solar cell at different concentration levels [61]

X	LM		MM	
	$1/\eta \, d\eta/dT$ (%/K)	$1/V_{oc} \, dV_{oc}/dT$ (%/K)	$1/\eta \, d\eta/dT$ (%/K)	$1/V_{oc} \, dV_{oc}/dT$ (%/K)
1	-0.257	-0.241	-0.305	-0.272
100	-0.134	-0.160	-0.188	-0.184
250	-0.132	-0.143	-0.179	-0.172
500	-0.129	-0.129	-0.172	-0.162
750	-0.117	-0.126	-0.163	-0.151
1000	-0.109	-0.122	-0.157	-0.147

4 Equivalent Circuit Models of MJ Solar Cells

An MJ solar cell can be considered as several series connected p–n junctions. Each junction can be represented by an equivalent circuit model. The most frequently used models are the single exponential model (SEM) and the double exponential model (DEM) [59]. Figure 6 shows an example of the equivalent circuits of a TJ solar cell by connecting the three subcells circuits in series.

Taking into account the SEM model, the current density of each subcell can be mathematically expressed as follows:

$$J = J_{sc,i} - J_{0,i} \left(\exp^{\frac{(V_i + JR_{s,i})}{m_i V_T}} - 1 \right) - \frac{V_i + JR_{s,i}}{R_{p,i}} \quad (17)$$

where each i subcell is characterized by a set of five parameters: the short-current density ($J_{sc,i}$), the diode-saturation current density ($J_{0,i}$), the diode ideality factor (m_i), the series resistance ($R_{s,i}$), and the shunt (or parallel) resistance ($R_{p,i}$). V_T is the semiconductor thermal voltage given by $V_T = kT/q$.

Equation (17) combines the different recombination mechanisms into one diode term that takes place in an MJ solar cell. Bearing this in mind, the current density of each subcell can be more accurately expressed by the DEM model as shown:

$$J = J_{sc,i} - J_{01,i} \left(\exp^{\frac{(V_i + JR_{s,i})}{m_{1,i} V_T}} - 1 \right) - J_{02,i} \left(\exp^{\frac{(V_i + JR_{s,i})}{m_{2,i} V_T}} - 1 \right) - \frac{V_i + JR_{s,i}}{R_{p,i}} \quad (18)$$

where each i subcell is characterized by a set of seven parameters: the short-current density ($J_{sc,i}$), the diode-saturation current densities ($J_{01,i}$, $J_{02,i}$), the diode ideality factors ($m_{1,i}$, $m_{2,i}$), the series resistance ($R_{s,i}$), and the shunt resistance ($R_{p,i}$). The first diode term represents the surface and bulk region recombination, which usually dominates at high irradiance levels with $m_{1,i} \approx 1$, and the second diode term

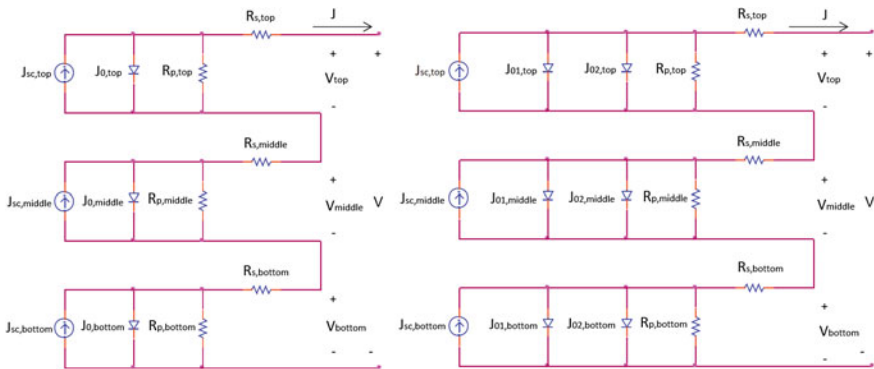


Fig. 6 Equivalent circuit models of a TJ solar cell by using the SEM (*left*) and the DEM (*right*)

represents the depletion region recombination, which usually dominates at low irradiance levels with $m_{2,i} \approx 2$ [57].

The total voltage of the MJ solar cell, neglecting the voltage decrease on the tunnel junctions [63], can simply be obtained by adding the voltages of each subcell as shown:

$$V = \sum_{i=1}^n V_i \quad (19)$$

The model's parameters described previously depend on the operating conditions, such as concentration and cell temperature, for the MJ solar cell [64]. At the same time, current MJ solar cells are usually fabricated monolithically and incorporate only two electrical terminals. Because of this, the separate measurement of the individual subcells and the determination of their parameters is a complex task [65]. Some investigators have proposed different methods to obtain the parameters of the subcells by making different assumptions and simplifications. Examples of extraction methods based on the SEM scheme can be found in the literature [46, 55, 59, 66–68] as can results from those based on the DEM scheme [59, 69–71]. It is important to note that these studies usually estimate the parameters at a particular set of operating conditions. Furthermore, the ability to translate the parameters at a desired operating condition is still challenging; thus the application of these models is often limited. Figure 7 shows an example of the modelled I-V characteristics of a typical GaInP/GaInAs/Ge device using Eqs. (17) and (19) by setting $R_{s,i} = 0$ and $m_i = 1$ under $1 \times$ concentration.

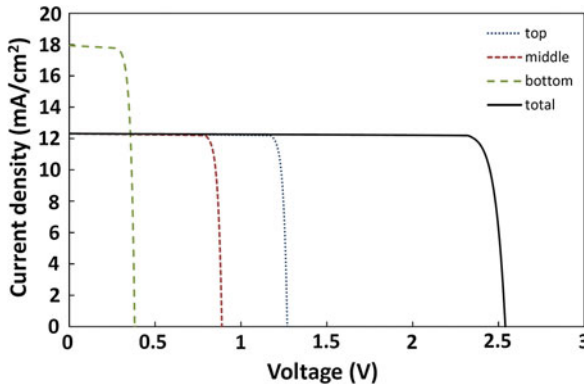


Fig. 7 Modelled I-V characteristics of each individual subcell and for the whole device of an LM GaInP/GaInAs/Ge solar cell under reference conditions (AM1.5D, ASTM G173-03, 1000 W/m², 25 °C)

5 Performance of MJ Solar Cells Under Real Operating Conditions

Currently the use of MJ solar cells for terrestrial applications is limited to HCPV due to their relatively high cost. HCPV technology is based on the use of less expensive optical elements to collect direct incidence sunlight and concentrate it to approximately $300\times$ to $2000\times$ on the surface of the solar cell. The aim is to decrease the cost of electricity, thus decreasing the semiconductor material by the use of the less expensive optics [72–75].

Under actual conditions, the performance of MJ solar cells in an HCPV system will be affected by time-varying atmospheric parameters. Therefore, it is necessary to quantify the impacts of the different phenomena to accurately estimate their performance. In this section, a discussion is presented on the main parameters that affect the behaviour of MJ solar cells outdoors. A procedure to quantify these parameters is addressed.

5.1 Thermal Factor

As presented in Sect. 3, the operating temperature of an MJ solar cell affects its electrical performance. Under real operating conditions, the cell temperature is not constant because it is affected by the changes in the direct normal irradiance (DNI), air temperature (T_{air}), and wind speed (W_s) [76, 77].

As already discussed, the effect of temperature on the electrical parameters of MJ solar cells can be quantified, with a low margin of error, using linear coefficients. Bearing this in mind, the effect of cell temperature on the power output can be quantified as shown:

$$\text{TF} = 1 - \gamma(T_c - T_c^*) \quad (20)$$

where TF is defined as the thermal factor (TF), γ is the maximum power temperature coefficient at the operating concentration, T_c is the cell temperature, and T_c^* is the cell temperature under reference conditions ($T_c^* = 25^\circ\text{C}$).

In contrast, direct measurement of the cell temperature in HCPV systems is a complex task due to the special features that arise because the cells are surrounded by different peripheral elements [78]. Because of this, the scientific community has devoted considerable effort to develop methods for indirectly predicting the cell temperature in HCPV devices from different parameters (i.e., atmospheric parameters and/or easily measurable parameters in the concentrator) [77]. Among the different procedures, the methods based on atmospheric parameters present the advantage of allowing estimation of the cell temperature for a specific location without directly measuring the concentrator. Because of this, they are a more useful

tool for the electrical characterization at a desired location if the atmospheric data are available.

A simple method based on linear coefficients as a function of DNI, T_{air} , and W_s has been proposed [76]. The procedure is based on the following relation as follows:

$$T_c = T_{\text{air}} + a_1 \text{DNI} + a_2 W_s \quad (21)$$

where a_1 and a_2 are specific coefficients of the concentrator. In addition, if we assume that the influence of W_s does not play an important role in the estimation of cell temperature, Eq. (21) can be simplified as:

$$T_c = T_{\text{air}} + a_1 \text{DNI} \quad (22)$$

A slightly more sophisticated expression as a function of the same atmospheric parameters has been proposed [79]. In this case, the cell temperature is obtained as follows:

$$T_c = T_{\text{air}} + b_1 \text{DNI} \left(\exp \left(-\frac{W_s}{2W_0} \right) + b_2 \right) \quad (23)$$

where b_1 , b_2 , and W_0 are specific coefficients of the concentrator. As in the previous relations, the method assumes that the cell temperature is proportional to DNI, but it uses an exponential correction based on the wind speed.

5.2 Spectral Factor

As was discussed in Sect. 3, the performance of MJ solar cells shows strong spectral dependence. Furthermore, the spectral distribution of incident irradiance is affected by atmospheric parameters and changes during the course of day, month, or year. In particular, the atmospheric parameters with the largest influence on the spectral irradiance and on the performance of MJ solar cells are, in order of importance, AM, aerosol optical depth (usually quantified at 500 or 550 nm), and precipitable water [80–84].

As was also mentioned, the performance of MJ solar cells under spectral variation is mainly determined by the current balance among the subcells. This effect can be quantified through the spectral factor (SF) as [84]:

$$\text{SF} = \frac{\min(J_{\text{sc},i} E_b(\lambda)) \int E_{b,\text{ref}}(\lambda) d\lambda}{\min(J_{\text{sc},i}(E_{b,\text{ref}}(\lambda))) \int E_b(\lambda) d\lambda} \quad (24)$$

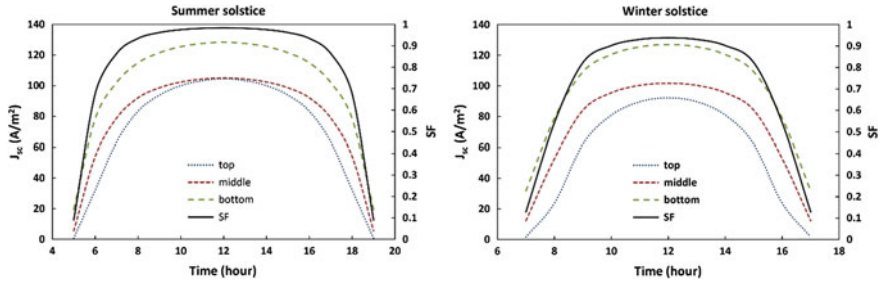


Fig. 8 Simulated SF and short-circuit current densities of an LM GaInP/GaInAs/Ge solar cell with an SOG Fresnel lens as a primary optic at the summer and winter solstices in Granada, southern Spain. The other parameters are kept constant at the reference values defined by the AM1.5D, ASTM G-173-03 reference spectrum [30]

where the short-circuit current density of each i junction in a concentrator is given by:

$$J_{sc,i} = \int E_b(\lambda) \eta_{opt}(\lambda) SR_i(\lambda) d\lambda \quad (25)$$

where $E_b(\lambda)$ is the incident direct normal spectral distribution, $E_{b,ref}(\lambda)$ is the direct reference spectrum, and $\eta_{opt}(\lambda)$ is the optical efficiency of the concentrator.

Equation (24) evaluates the performance of an MJ solar cell as a function of the mismatch among the short-circuit current densities of the different junctions relative to the value obtained under illumination by the reference spectrum. To explain this in more detail, Fig. 8 shows the simulated SF and short-circuit current densities of

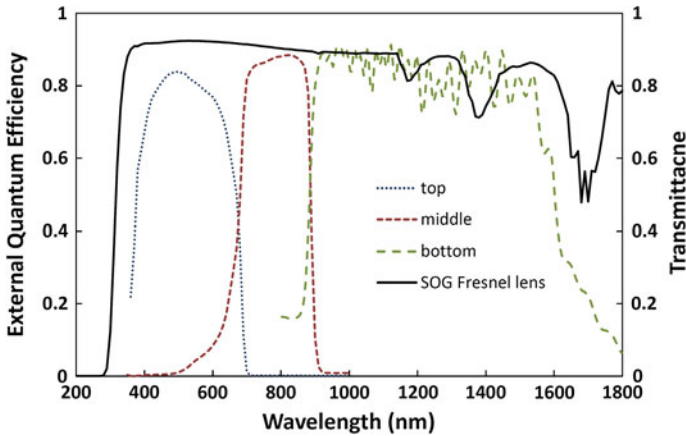


Fig. 9 External quantum efficiency of an LM GaInP/GaInAs/Ge solar cell and the transmittance of an SOG Fresnel lens. Refer to this plot, together with the solar spectrum shown in Fig. 2, for the discussion and results found in this section

each junction for an LM GaInP/GaInAs/Ge solar cell with a silicone-on-glass (SOG) Fresnel lens as a primary optic (see Fig. 9 for the EQE and transmittance) for 2 example days at Granada, southern Spain. The complete procedure followed is explained in detail in the next subsection.

To show a contrasting variation between data, the summer and winter solstices were selected as shown in Fig. 8. These days represent the minimum and maximum daily average AM values, respectively. As can be seen, the behaviour of the SF is similar for both days. The maximum spectral losses are produced at sunrise and sunset when the AM values are greater, and the minimum spectral losses are produced at midday when the AM values are lower. Although the behaviour of the SF is similar on both days, the spectral losses are significantly greater on the winter solstice than at the summer solstice with average SF values of approximately 0.7 and 0.8, respectively. This difference can be explained by taking into account that the AM values are significantly greater at the winter solstice than at the summer solstice. This can be also observed from the analysis of the short-circuit current densities of the top and middle junctions. As can be seen for low AM values, the top and middle junctions yield similar currents. However, for high AM values, the top junction strongly limits the current, thus resulting in an overall decrease of the SF of the MJ solar cell [80, 84].

5.3 Power Output

The power output of the cell is a key parameter because it allows knowledge of the energy yield of a particular photovoltaic device. The power produced by an MJ solar cell as a function of the incident DNI can be expressed as shown:

$$P = \text{DNI} \cdot A_{\text{cell}} \cdot X \cdot \eta_{\text{cell}} \quad (26)$$

where η_{cell} is the efficiency of the cell at the operating concentration, and other conditions are held at the reference conditions. The effective concentration can be related to the geometric concentration (C_{geo}) of the HCPV device as shown:

$$X = \eta_{\text{opt}} \cdot C_{\text{geo}} \quad (27)$$

where geometric concentration is defined as:

$$C_{\text{geo}} = \frac{A_{\text{lens}}}{A_{\text{cell}}} \quad (28)$$

where A_{lens} is the area of the primary optics, A_{cell} is the area of the cell, and η_{opt} is the optical efficiency.

By itself, Eq. (26) neglects the cell temperature and spectral effects. Combining Eqs. (20), (24), and (26), the power generated by an MJ solar cell can be more accurately expressed as:

$$P = \text{DNI} \cdot A_{\text{cell}} \cdot \eta_{\text{opt}} \cdot C_{\text{geo}} \cdot \eta_{\text{cell}} \cdot \text{TF} \cdot \text{SF} \quad (29)$$

This equation estimates the power output of an MJ solar cell in a concentrator as a function of its temperature and direct normal incidence characterized by its irradiance (W/m^2) and spectral distribution.

Figure 12 shows an example of the simulated annual power density of an MJ solar cell with an SOG Fresnel lens as a primary optic in Granada, southern Spain. The external quantum efficiency of the cell and transmittance of the Fresnel lens used are plotted in Fig. 9. The system has a geometric concentration of $700\times$, an optical efficiency of 85 %, and a cell efficiency under reference conditions of 38.5 %.

To quantify the effect of cell temperature, the times series of air temperature is estimated from the maximum, minimum, and average values obtained from the NASA atmospheric database for an entire year [85–87]. The cell temperature was calculated using Eq. (22) from the air temperature and considering $a_1 = 0.06 \text{ } ^\circ\text{C/Wm}^{-2}$. Once the cell temperature is obtained, the TF is estimated using Eq. (20) and by taking $\gamma = -0.12 \text{ } \%/^\circ\text{C}$ as shown in Fig. 10.

The spectral distribution of the direct normal irradiance for the whole year was simulated using the simple model of the atmospheric radiative transfer of sunshine (SMARTS) [88]. The AM was calculated as a function of the Sun's zenith angle (θ) as [89]:

$$\text{AM} = \frac{1}{\cos \theta + 0.45665\theta^{0.07}(96.4836 - \theta)^{-1.697}} \quad (30)$$

and the monthly average values of aerosol optical depth at 550 nm and precipitable water were gathered from the Aerosol Robotic Network data set [90]. In addition, Granada is a nonindustrialized medium-size city; therefore, the rural aerosol model

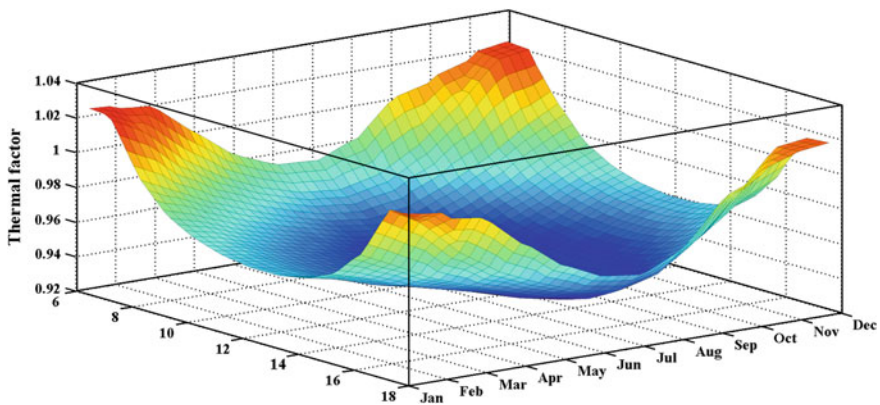


Fig. 10 Simulated annual TF for an LM GaInP/GaInAs/Ge solar cell with an SOG Fresnel lens as primary optics in Granada, southern Spain. The system has a geometric concentration of $700\times$, an optical efficiency of 85 %, and a cell efficiency under reference conditions of 38.5 %

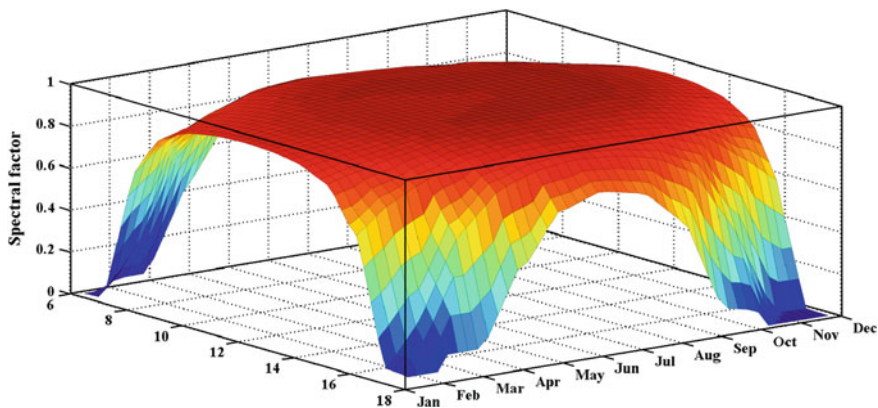


Fig. 11 Simulated annual SF for an LM GaInP/GaInAs/Ge solar cell with an SOG Fresnel lens as primary optics in Granada, southern Spain. The system is the same as the one described for Figs. 10 and 12

was selected. The rest of the input parameters for the SMARTS model were held constant at their reference values defined by the standard AM1.5D, ASTM G-173-03 at which MJ solar cells and HCPV devices are rated [30]. Once the spectral distribution is available, the SF was obtained using Eqs. (24) and (25), and the data for the external quantum efficiency and lens transmittance shown in Fig. 9. The result is shown in Fig. 11.

Finally, the power density of the cell per unit area is predicted using Eq. (29) every 10 min for the whole year as a function of the simulated DNI, TF, and SF values. This is shown in Fig. 12. In this figure, the generated power density ranges

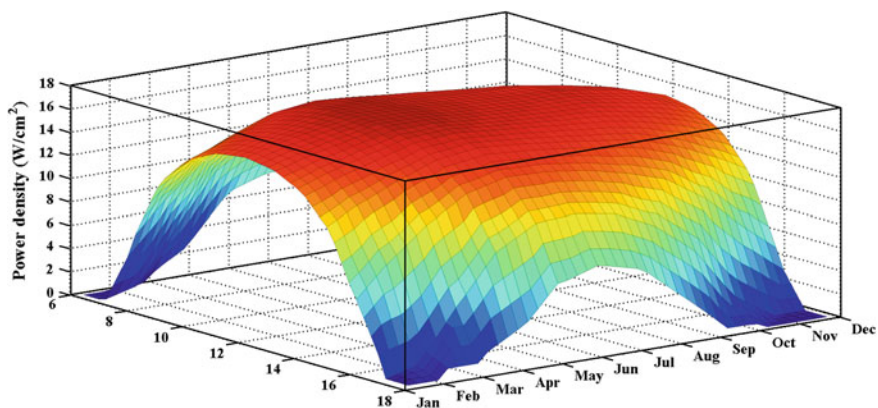


Fig. 12 Simulated annual power density for an LM GaInP/GaInAs/Ge solar cell with an SOG Fresnel lens as primary optics in Granada, southern Spain. The calculation utilized (Eq. 29) and the results shown in Figs. 10 and 11

from 0 to 18 W/cm^2 and is dominated by the incident DNI. In contrast, the TF and the SF lead to power losses as can be seen in Figs. 10 and 11. In particular, the SF ranges from 0 to 1, whereas the TF ranges from 0.9 to 1. Based on this, it could be concluded that the spectral effects produce greater energy losses than the temperature effects. However, as can be seen in Fig. 10, the maximum thermal losses are produced at midday and at summer months when the contribution to the final annual energy yield is at a maximum. In contrast, as can be seen in Fig. 11, the maximum spectral losses are produced at sunrise and sunset and at winter months when the contribution to the annual energy yield is lower than in the previous case. This implies that the spectral losses do not necessarily dominate the energy losses of an MJ solar cell in a concentrator under real operating conditions for a particular period of time. To analyse the factor that leads to greater energy losses, the TF and SF terms of Eq. (29) must be carefully analysed and compared. Thermal and spectral losses change during the course of a day, month, or year and for each location. Consequently, this type of analysis should be performed for a given period of time and a specific location to accurately analyse and quantify the impact of the spectral and thermal effects on the energy harvested.

The procedure based on Eq. (29) described previously for estimating the maximum power of an HCPV device was evaluated at the Centre of Advanced Studies in Energy and Environment at the University of Jaen in Southern Spain. The electrical parameters of an HCPV module were monitored together with the main atmospheric parameters during the course of 2 years (2013–2014). The HCPV module was made up of 20 TJ LM GaInP/GaInAs/Ge solar cells with an area of 0.763 cm^2 interconnected in series and each with the EQE shown in Fig. 9. The module used SOG Fresnel lenses with the transmittance shown in Fig. 9 as a primary optical element. The secondary optical element for each cell consisted of a

Fig. 13 Schematic diagram of a single receiver of the HCPV module under study

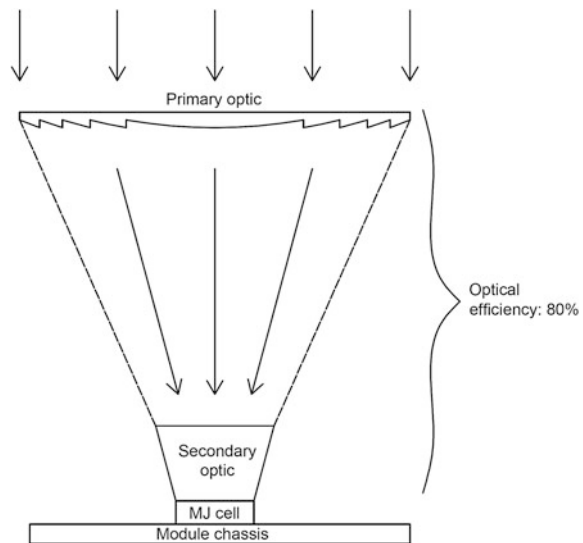


Table 3 RMSE, MBE, and R^2 between actual and predicted output power for an HCPV MJ cell

RMSE (%)	MBE (%)	R^2
3.46	-1.26	0.98

truncated pyramid reflective cup that used an aluminium film layer to enhance its reflectivity. The module had a geometric concentration of $700\times$ and used passive cooling to ensure that MJ solar cells operate at their optimal operation range, which is $50\text{--}80\text{ }^{\circ}\text{C}$. The module had a nominal maximum power of 280 W under reference conditions ($\text{DNI} = 1000\text{ W/m}^2$, $T_C = 25\text{ }^{\circ}\text{C}$, spectrum = AM1.5D) [91]. Figure 13 shows a schematic diagram of a single receiver of the HCPV module under study.

Table 3 shows the root mean square error (RMSE), the mean bias error (MBE), and the determination coefficient (R^2) between actual and predicted data. This shows that the procedure described above is valid for estimating the maximum power of an HCPV device at a particular location if high-quality atmospheric parameters are available.

6 Conclusions

MJ concentrator solar cells are complex devices because they consist of several devices stacked in optical and electrical series. This allows them to reach efficiencies that are not possible with SJ devices. The analysis of their behavior, however, is still possible from consideration of their external quantum efficiency, band-gaps, and temperature coefficients of individual subcells. This allows the influence of the input spectrum to be considered so that the short-circuit current, open circuit voltage, and FF can nonetheless be understood as a function of temperature, input spectrum, and irradiance that is a result of the optical concentration factor. A lumped parameter approach that considers a TF and an SF allows the estimation of the power output for real HCPV systems. These factors, when combined with atmospheric and meteorological data, allow for the calculation of the power output as a function of time of day and time of year.

Future work can consider this approach for different geographic locations and for several complex conditions faced by real HCPV systems in the field. The analysis can also be expanded to consider lattice-MM and other device structures such as the IMM. Not considered in the above basic description is the effect of transient irradiance, partial shadowing or cell mismatching. This can also be considered in more complex modelling efforts. The general conclusion is that the behaviour of MJ concentrator solar cells and modules can, and must, be understood from a fundamental perspective for large-scale HCPV deployment to be successfully undertaken.

References

1. Philipps S, Dimroth F, Bett A (2013) In: McEvoy A, Castañer L, Markvart T (eds) Solar cells: materials, manufacture and operation. Elsevier, Amsterdam, p 353
2. Bailey S, Raffaele R (2012) In: McEvoy AMT, Castañer L (eds) Practical handbook of photovoltaics fundamentals and applications. Elsevier, Boston, p 863
3. Algora C In: Luque A, Andreev V (eds) Concentrator photovoltaics. Springer, Berlin, p 89
4. Olson J, Friedman D, S Kurtz (2003) In: Luque A, Hegedus S (eds) Handbook of photovoltaic science and engineering. Wiley, New York, p 359
5. Fraas L (2014) Low-cost solar electric power. Springer, Cham, p 97
6. Kurtz S, Geisz J (2010) Multijunction solar cells for conversion of concentrated sunlight to electricity. *Opt Express* 18(9):A73–A78
7. King R, Shusari D, Larrabee D, Liu X-Q, Rehder E, Edmondson K, Cotal H, Jones R, Ermer J, Fetzer C, Law D, Karam N (2012) Solar cell generations over 40 % efficiency. *Prog Photovolt Res Appl* 20:801–815
8. Tanabe K (2009) A review of ultrahigh efficiency III-V semiconductor compound solar cells: multijunction tandem, lower dimensional, photonic up/down conversion and plasmonic nanometallic structures. *Energies* 2:504–530
9. Wilt D, Stan M (2012) High efficiency multijunction photovoltaic development. *Ind Eng Chem Res* 51(37):11931–11940
10. Landsberg P, Markvart T (2013) In: McEvoy A, Castañer L, Markvart T (eds) Solar cells: materials, manufacture and operation. Elsevier, Amsterdam, p 55
11. de Vos A (1992) Endoreversible thermodynamics of solar energy conversion. Oxford University Press, New York, p 120
12. Smestad G, Ries H (1992) Luminescence and current-voltage characteristics of solar cells and optoelectronic devices. *Sol Energy Mater Sol Cells* 25:51–71
13. Smestad G (2002) Optoelectronics of Solar Cells. SPIE, Bellingham, p 57
14. Tobin S, Vernon S, Bajgar C, Wojtczuk SJ, Melloch M, Keshavarzi A, Stellwag T, Venkatesan S, Lundstrom M, Emery K (1990) Assessment of MOCVD and MBE growth GaAs for high-efficiency solar cell applications. *IEEE Trans Electron Devices* 37(2):469–477
15. Ptak A, Johnston S, Kurtz S, Friedman D, Metzger W (2003) A comparison of MBE- and MOCVD-grown GaInNAs. *J Cryst Growth* 251(1–4):392–398
16. Bett A, Adelhelm R, Agert C, Beckert R, Dimroth F, Schubert U (2001) Advanced III-V solar cell structures grown by MOVPE. *Sol Energy Mater Sol Cells* 66(1–4):541–550
17. Jackrel D, Bank S, Yuen H, Wistey M, Harris J, Ptak A, Johnston S, Friedman D, Kurtz S (2007) Dilute nitride GaInNAs and GaInNAsSb solar cells by molecular beam epitaxy. *J Appl Phys* 101(11):114916
18. Malik R (1989) III-V semiconductor materials and devices. Elsevier, Amsterdam
19. Simon MS, Kwok KN (2006) Physics of semiconductor devices. Wiley, New York
20. Levinshtein ME, Rumyantsev SL, Shur MS (2001) Properties of advanced semiconductor materials: GaN, AlN, InN, BN, SiC, SiGe. Wiley, New York
21. Green M (2003) Third generation photovoltaics. Springer, Berlin
22. Mokkapati S, Jagadish C (2009) III-V compound SC for optoelectronic devices. *Mater Today* 12(4):22–32
23. Washburn J, Kvam EP, Liliental-Weber Z (1991) Defect formation in epitaxial crystal growth. *J Electron Mater* 20(2):155–161
24. Cohen M, Bergstresser T (1966) Band structures and pseudopotential form factors for fourteen semiconductors of the diamond and zinc-blende structures. *Phys Rev* 141(2):789–796
25. Yamaguchi M, Takamoto T, Araki K, Ekins-Daukes N (2005) Multi-junction III-V solar cells: current status and future potential. *Sol Energy* 79(1):78–85
26. Dimroth F (2006) High-efficiency solar cells from III-V compound semiconductors. *Physica Status Solidi C: Conf* 3(3):373–379

27. King R, Bhusari D, Larrabee D, Liu X-Q, Rehder E, Edmondson K, Cotal H, Jones R, Ermer J, Fetzer C, Law D, Karam N (2012) Solar cell generations over 40% efficiency. *Prog Photovolt Res Appl* 20(6):801–815
28. Walker A, Thériault O, Wilkins M, Wheeldon J, Hinzer K (2013) Tunnel-junction-limited multijunction solar cell performance over concentration. *IEEE J Sel Topics Quantum Electron* 19(5):1–8
29. Guter W, Schöne J, Philipps S, Steiner M, Siefert G, Wekkeli A, Welser E, Oliva E, Bett A, Dimroth F (2009) Current-matched triple-junction solar cell reaching 41.1 % conversion efficiency under concentrated sunlight. *Appl Phys Lett* 54(22)
30. ASTM G 173-03e1 (2012) Standard tables for reference solar spectral irradiance: direct normal and hemispherical on 37 tilted surface
31. Cotal H, Fetzer C, Boisvert J, Kinsey G, King R, Hebert P, Yoon H, Karam N (2009) III-V multijunction solar cells for concentrating photovoltaics. *Energy Environ Sci* 2(2):174–192
32. García I, Rey-Stolle I, Galiana B, Algorta C (2009) A 32.6 % efficient lattice-matched dual-junction solar cell working at 1000 suns. *Appl Phys Lett* 94(5):0535509
33. Araki K, Yamaguchi M, Kondo M, Uozumi H (2003) Which is the best number of junctions for solar cells under ever-changing terrestrial spectrum? In: 3rd World conference on photovoltaic energy conversion, pp 307–312
34. Yoon H, Haddad M, Mesropian S, Yen J, Edmondson K, Law D, King R, Bhusari D, Boca A, Karam N (2008) Progress of inverted metamorphic III-V solar cell development at Spectrolab. In: 33rd IEEE photovoltaic specialists conference
35. Geisz J, Kurtz S, Wanlass M, Ward J, Duda A, Friedman D, Olson J, McMahon W, Moriarty T, Kiehl J (2007) High-efficiency GaInPGaAsInGaAs triple-junction solar cells grown inverted with a metamorphic bottom junction. *Appl Phys Lett* 91(2):023502–023502
36. Geisz J, Friedman D, Ward J, Duda A, Olavarria W, Moriarty T, Kiehl J, Romero M, Norman A, Jones K (2008) 40.8 % efficient inverted triple-junction solar cell with two independently metamorphic junctions. *Appl Phys Lett* 93(12):123505
37. King R, Law D, Edmondson K, Fetzer C, Kinsey G, Yoon H, Krut D, Ermer J, Sherif R, Karam N (2007) Advances in high-efficiency III-V multijunction solar cells. *Adv Optoelectron*
38. Tanabe K, Fontcuberta i Morral A, Atwater H, Aiken D, Wanlass M (2006) Direct-bonded GaAs/InGaAs tandem solar cell. *Phys Lett* 89(10):102106
39. Derendorf K, Essig S, Oliva E, Klinger V, Roesener T, Philipps S, Benick J, Hermle M, Schachtner M, Siefert G, Jäger W, Dimroth F (2013) Fabrication of GaInP/GaAs//Si solar cells by surface activated direct wafer bonding. *IEEE J Photovolt* 3(4):1–6
40. Häussler D, Houben L, Essig S, Kurttepli M, Dimroth F, Dunin-Borkowski R, Jäger W (2013) Aberration-corrected transmission electron microscopy analyses of GaAs/Si interfaces in wafer-bonded multi-junction solar cells. *Ultramicroscopy* 134:55–61
41. Dimroth F, Grave M, Beutel P, Fiedeler U, Karcher C, Tibbits T, Oliva E, Siefert G, Schachtner M, Wekkeli A, Bett A, Krause R, Piccin M, Blanc N, Drazek C, Guiot E, Ghyselen B, Salvatet T, Tauzin A, Signamarcheix T (2014) Wafer bonded four-junction GaInP/GaAs//GaInAsP/GaInAs concentrator solar cells with 44.7 % efficiency". *Prog Photovolt Res Appl* 22(3):277–282
42. Varshni YP (1967) Temperature dependence of the energy gap in semiconductors. *Physica* 34:149–154
43. Aiken D, Stan M, Murray C, Sharps P, Hills J, Clevenger B (2002) Temperature dependent spectral response measurements for III-V multi-junction solar cells. In: 29th conference record of the IEEE photovoltaic specialists conference
44. Helmers H, Schachtner M, Bett A (2013) Influence of temperature and irradiance on triple-junction solar subcells. *Sol Energy Mater Sol Cells* 116:144–152
45. Braun A, Katz EGJ (2013) Basic aspects of the temperature coefficients of concentrator solar cell performance parameters. *Prog Photovolt Res Appl* 21(5):1087–1094

46. Domínguez C, Antón I, Sala G (2010) Multijunction solar cell model for translating I-V characteristics as a function of irradiance, spectrum, and cell temperature. *Prog Photovolt Res Appl* 18(4):272–284
47. Friedman D (1996) Modelling of tandem cell temperature coefficients. In: 25th conference record of the IEEE photovoltaic specialists conference
48. Meusel M, Baur C, Létay G, Bett A, Warta W, Fernandez E (2003) Spectral response measurements of monolithic GaInP/Ga(In)As/Ge triple-junction solar cells: measurement artifacts and their explanation. *Prog Photovolt Res Appl* 11(8):499–514
49. Fernández E, Loureiro A, Higuera P, Siefer G (2011) Monolithic III-V triple-junction solar cells under different temperatures and spectra. In: Proceedings of the 8th spanish conference on electron devices, CDE'2011, Art no 5744222
50. Baudrit M, Algorta C (2008) Modeling of GaInP/GaAs dual-junction solar cells including tunnel junction. In: 33rd IEEE photovoltaic specialists conference
51. Siefer G, Baur C, Bett A (2010) External quantum efficiency measurements of Germanium bottom subcells: measurement artifacts and correction procedures. In: 35th IEEE Photovoltaic Specialists Conference
52. Faine P, Kurtz S, Riordan C, Olson J (1991) The influence of spectral solar irradiance variations on the performance of selected single-junction and multijunction solar cells. *Solar Cells* 31(3):259–278
53. Domínguez C, Anton I, Sala G, Askins S (2013) Current-matching estimation for multijunction cells within a CPV module by means of component cells. *Prog Photovolt Res Appl* 21(7):1478–1488
54. McMahon W, Emery K, Friedman D, Ottoson L, Young M, Ward J, Kramer C, Duda A, Kurtz S (2008) Fill factor as a probe of current-matching for GaInP/GaAs tandem cells in a concentrator system during outdoor operation. *Prog Photovolt Res Appl* 16(3):213–224
55. Fernández E, Siefer G, Almonacid F, Loureiro A, Pérez-Higuera P (2013) A two subcell equivalent solar cell model for III-V triple junction solar cells under spectrum and temperature variations. *Sol Energy* 92:221–229
56. Meusel M, Adelhelm R, Dimroth F, Bett A, Warta W (2002) Spectral mismatch correction and spectrometric characterization of monolithic III-V multi-junction solar cells. *Prog Photovolt Res Appl* 10(4):243–255
57. Siefer G, Bett A (2014) Analysis of temperature coefficients for III-V multijunction concentrator cells. *Prog Photovolt Res Appl* 22(5):515–524
58. Kinsey G, Hebert P, Barbour K, Krut D, Cotal H, Sherif R (2008) Concentrator multifunction solar cell characteristics under variable intensity and temperature. *Prog Photovolt Res Appl* 16(6):503–508
59. Segev G, Mittelman G, Kribus A (2012) Equivalent circuit models for triple-junction concentrator solar cells. *Sol Energy Mater Sol Cells* 98:57–65
60. Braun A, Hirsch B, Vossier A, Katz E, Gordon J (2013) Temperature dynamics of multijunction concentrator solar cells up to ultra-high irradiance. *Prog Photovolt Res Appl* 21(2):202–208
61. Fernández E, Siefer G, Schachtner M, García Loureiro A, Pérez-Higuera P (2012) Temperature coefficients of monolithic III-V triple-junction solar cells under different spectra and irradiance levels. *AIP Conf Proc* 1477:189–193
62. Siefer G, Baur C, Meusel M, Dimroth F, Bett A, Warta W (2002) Influence of the simulator spectrum on the calibration of multi-junction solar cells under concentration. In: 29th IEEE photovoltaic specialists conference
63. Guter W, Bett A (2006) I-V characterization of tunnel diodes and multijunction solar cells. *IEEE Trans Electron Devices* 53(9):2216–2222
64. Ben Or A, Appelbaum J (2014) Dependence of multi-junction solar cells parameters on concentration and temperature. *Solar Energy Mater Solar Cells* 130:234–240
65. Karcher C, Helmers H, Schachtner M, Dimroth F, Bett A (2014) Temperature-dependent electroluminescence and voltages of multi-junction solar cells. *Prog Photovolt Res Appl* 22(7):757–763

66. Wanlass M, Emery K, Gessert T, Horner G, Osterwald C, Coutts T (1989) Practical considerations in tandem cell modeling. *Solar Cells* 27(1–4):191–204
67. Ben Or A, Appelbaum J (2013) Estimation of multi-junction solar cell parameters. *Prog Photovolt Res Appl* 21(4):713–723
68. Ben Or A, Appelbaum J (2013) Performance analysis of concentrator photovoltaic dense-arrays under non-uniform irradiance. *Solar Energy Mater Solar Cells* 117:110–119
69. Reinhardt K, Lewis B, Kreifels T (2000) Multijunction solar cell iso-junction dark current study. In 28th IEEE photovoltaic specialists conference
70. Nishioka K, Takamoto T, Agui T, Kaneiwa M, Uraoka Y, Fuyuki T (2005) Evaluation of temperature characteristics of high-efficiency InGaP/InGaAs/Ge triple-junction solar cells under concentration. *Sol Energy Mater Sol Cells* 85(3):429–436
71. Nishioka K, Suetō T, Uchida M, Ota Y (2010) Detailed analysis of temperature characteristics of an InGaP/InGaAs/Ge triple-junction solar cell. *J Electron Mater* 39(6):704–708
72. Zubi G, Bernal-Agustín J, Fracastoro G (2009) High concentration photovoltaic systems applying III-V cells. *Renew Sustain Energy Rev* 13(9):2645–2652
73. Pérez-Higueras P, Muñoz E, Almonacid G, Vidal P (2011) High concentrator photovoltaics efficiencies: present status and forecast. *Renew Sustain Energy Rev* 15(4):1810–1815
74. Fernández E, Pérez-Higueras P, García Loureiro A, Vidal P (2013) Outdoor evaluation of concentrator photovoltaic systems modules from different manufacturers: first results and steps. *Prog Photovolt Res Appl* 21(4):693–701
75. Luque A, Sala G, Luque-Heredia I (2006) Photovoltaic concentration at the onset of its commercial deployment. *Prog Photovolt Res Appl* 14(5):413–428
76. Almonacid F, Pérez-Higueras P, Fernández E, Rodrigo P (2012) Relation between the cell temperature of a HCPV module and atmospheric parameters. *Sol Energy Mater Sol Cells* 105:322–327
77. Rodrigo P, Fernández E, Almonacid F, Pérez-Higueras P (2014) Review of methods for the calculation of cell temperature in high concentration photovoltaic modules for electrical characterization. *Renew Sustain Energy Rev* 38:478–488
78. Fernandez EF, Almonacid F, Rodrigo P, Pérez-Higueras P (2014) Calculation of the cell temperature of a high concentrator photovoltaic (HCPV) module: a study and comparison of different methods. *Sol Energy Mater Sol Cells* 121:144–151
79. Hornung T, Steiner M, Nitz P (2012) Estimation of the influence of Fresnel lens temperature on energy generation of a concentrator photovoltaic system. *Solar Energy Mater Solar Cells* 333–338:99
80. Kinsey G, Edmondson KM (2009) Spectral response and energy output of concentrator multijunction solar cells. *Prog Photovolt Res Appl* 17(5):279–288
81. Philipps S, Peharz G, Hoheisel R, Hornung T, Al-Abbadi N, Dimroth F, Bett A (2010) Energy harvesting efficiency of III-V triple-junction concentrator solar cells under realistic spectral conditions. *Sol Energy Mater Sol Cells* 94(5):869–877
82. Chan N, Brindley H, Ekins-Daukes N (2013) Impact of individual atmospheric parameters on CPV system power, energy yield and cost of energy. *Prog Photovolt Res Appl* 22(10):1080–1095
83. Chan N, Young TB, Brindley HE, Ekins-Daukes N, Araki K, Kemmoku YY (2012) Validation of energy prediction method for a concentrator photovoltaic module in Toyohashi Japan. *Prog Photovolt Res Appl* 21:1598–1610
84. Fernández E, Almonacid F, Ruiz-Arias JS-MA (2014) Analysis of the spectral variations on the performance of high concentrator photovoltaic modules operating under different real climate conditions. *Sol Energy Mater Sol Cells* 127:179–187
85. Surface meteorology and Solar Energy. Available: <https://eosweb.larc.nasa.gov/sse/>
86. Erbs D, Klein S, Beckman WA (1983) Estimation of degree-days and ambient temperature bin data from monthly-average temperatures. *Ashrae J* 25:60–65
87. Almonacid F, Pérez-Higueras P, Rodrigo P, Hontoria L (2013) Generation of ambient temperature hourly time series for some Spanish locations by artificial neural networks. *Renew Energy* 51:285–291

88. Gueymard C (2001) Parameterized transmittance model for direct beam and circumsolar spectral irradiance. *Sol Energy* 71(5):325–346
89. Kasten F, Young AT (1989) Revised optical air mass tables and approximation formula. *Appl Opt* 28(22):4735–4738
90. Aerosol Robotic Network. Available: <http://aeronet.gsfc.nasa.gov/>
91. IEC (2013) IEC 62670-1 ed1.0 Photovoltaic concentrators (CPV)—performance testing—part 1: standard conditions

High Concentrator Photovoltaics
Fundamentals, Engineering and Power Plants
Pérez-Higueras, P.; Fernández, E.F. (Eds.)
2015, IX, 477 p. 217 illus., Hardcover
ISBN: 978-3-319-15038-3